Improved estimation of the directional wave spectrum from marine radar images by employing a directional modulation transfer function (MTF)

Susanne Støle-Hentschel[a,b,*], Ruben Carrasco[c], José Carlos Nieto-Borge[d], Jörg Seemann[c] and Yaron Toledo[a]

[a] *Tel-Aviv University, School of Mechanical Engineering, Tel Aviv Yafo, Israel*
[b] *Université Paris-Saclay, ENS Paris-Saclay, Paris-Saclay, France*
[c] *Helmholtz-Zentrum Hereon, Ocean Surface Dynamics, Geesthacht, Germany*
[d] *Universidad de Alcalá, Department of Physics and Mathematics, Alcalá de Henares, Spain*

ARTICLE INFO

Keywords:
directional wave spectra
marine X-band radar
modulation transfer function (MTF)
directional MTF
2d–MTF
shadowing

ABSTRACT

This study focuses on improving the accuracy of the energy distribution in directional wave spectra from temporal sequences of marine radar images. Wave spectra are obtained by converting the image spectrum to a wave spectrum by employing a modulation transfer function (MTF). While the imaging mechanism in the plane of the radar beam has received much attention, the effect of the combination of different beam positions has been largely neglected. Herein, we demonstrate that any MTF can only be valid for a limited azimuthal coverage. However, the proposed directional MTF is well suited for small windows for which it corrects the relative projection between the average radar beam position and the wavenumber vector. Spectra of different sea states are compared, using the derived MTF and the established MTF. The analysis shows a significant improvement in the energy distribution in the directional wave spectra when the directional spreading is high. It is suggested that future work should aim to remove the necessary restriction to small windows by synthesizing the full directional spectrum from multiple small windows in different directions. In this way, marine radars are suitable to better reproduce sea states with extreme directional spreading, including multi-modal seas.

1. Introduction

Directional wave spectra represent sea state characteristics that are relevant to a wide range of applications. They are the standard representation of waves in forecasting systems and are therefore crucial in the calculation of load effects on structures. Measuring the evolution of directional wave spectra is also key in understanding the coupling of the air–sea interface and the related exchange of mass and momentum (Romero, Melville and Kleiss, 2012; Lenain and Melville, 2017). Traditionally, the standard method for obtaining sea state characteristics is based on buoy measurements. As the buoy is a single point device, the directional distribution of the spectral energy can only be obtained assuming a prescribed model (Longuet-Higgins, 1963; Lygre and Krogstad, 1986; Capon, Greenfield and Kolker, 1967; Barstow, Bidlot, Caires, Donelan, Drennan, Dupuis, Graber, Green, Gronlie, Guérin, Gurgel, Günther, Hauser, Hayes, Hessner, Hoja, Icard, Kahma, Keller, Krogstad, Lefevre, Lehner, Magnusson, Monbaliu, Nieto Borge, Pettersson, Plant, Quentin, Reichert, Reistad, Rosenthal, Saetra, Schulz-Stellenfleth, Walsh, Weill, Wolf, Wright and Wyatt, 2005; Lee, Jung and Haller, 2010; Lenain and Melville, 2017). Sea states do not generally obey the limits of such models, in particular in the presence multi-model seas, such as the combination of swell and windsea (Nieto Borge and Guedes Soares, 2000; Lund, Collins, Tamura and Graber, 2016).

Marine radars collect information over space and time simultaneously and can therefore deliver model-free directional wave spectra (Nieto Borge and Guedes Soares, 2000; Barstow et al., 2005; Ludeno, Orlandi, Lugni, Brandini, Soldovieri and Serafino, 2013; Wyatt, Green, Gurgel, Borge, Reichert, Hessner, Günther, Rosenthal, Saetra and Reistad, 2003), which have been proven suitable to capture the characteristics of directional sea states (Nieto Borge and Guedes Soares, 2000; Ludeno et al., 2013; Wyatt et al., 2003).

sstolehe@ens-paris-saclay.fr (S. Støle-Hentschel)
ORCID(s):

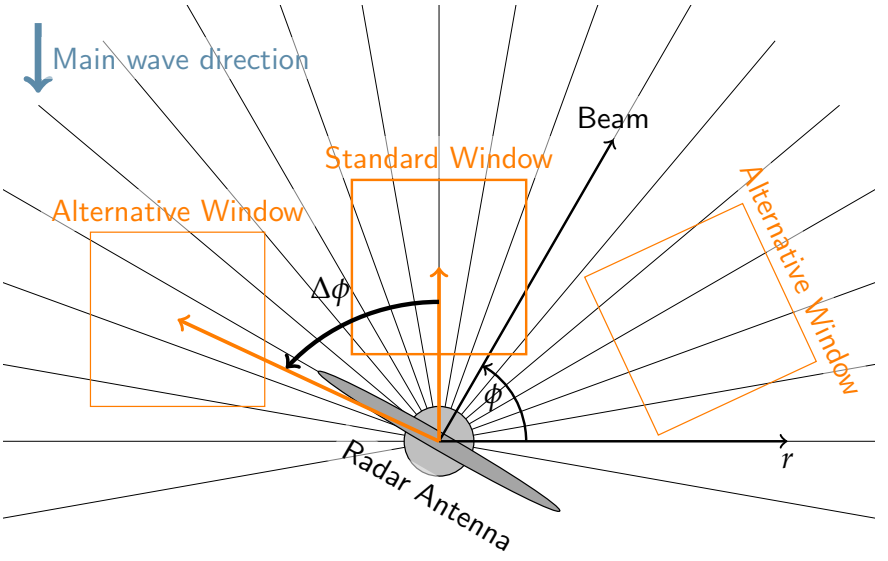

Figure 1: Illustration of the data acquisition by a radar. The antenna rotates, and hence, each azimuth position of the radar beam results in a different projection of the imaged waves. The standard window of observation is located against the main wave direction. Other positions are possible, e.g. the two alternative windows. The origin of the coordinate system is defined in the mean sea level for z-component and in the center of the radar antenna for the horizontal components ($r = \sqrt{x^2 + y^2}, \phi = \arctan(y/x)$). The position of the window is defined by the average azimuth angle of all grid points within one window ($\overline{\phi}$). The relative deviation from the standard window ($\overline{\phi} = \pi/2$) is denoted $\Delta\phi = \bar{\phi} - \pi/2$.

Nevertheless, the interpretation of the results can be limited owing to the influence of the imaging mechanisms that are not fully understood (Al-Habashneh, Moloney, Gill and Huang, 2015). The state–of–the–art algorithm for processing the radar backscatter involves the conversion from the imaging domain to the spectral domain by the modulation transfer function (MTF) (Nieto Borge, Rodriguez, Hessner and Gonzalez, 2004). The MTF was first described for SAR images, such as described by Alpers and Hasselmann (1978). Alpers and Hasselmann suggest to compose the transfer function as the sum of a tilt and a hydrodynamic contribution. For the remaining study, the hydrodynamic contribution is neglected due to the dominance of the tilt modulation, as shown by Støle-Hentschel, Seemann, Nieto Borge and Trulsen (2018) for the same grazing conditions. In their study, the authors examined the backscatter of a coherent X-band radar with a fixed antenna pointing in the main wave direction. The phase shift between the Doppler and intensity signals was obtained from the analytic signal and found to be 90° in the near range, as expected for a tilt dominated imaging mechanism. The tilt modulation has previously been derived under the assumption that the radar beams scanning the surface of interest are parallel, meaning that the azimuth angle is constant. This assumption is valid for SAR imagery, where a sideways-looking radar moves over a large area. When developing a tilt MTF, it is important to only take into account the projection effect between the 'fixed' radar beam angle and each individual wave number vector. This corresponds to the relative angle between the observation window and the wave direction. As SAR images are not easily available, a lot of efforts were put into exploring the applicability of marine radars to retrieve ocean observations. Young, Rosenthal and Ziemer (1985) documented that directional wave spectra can be obtained by employing a three-dimensional Fourier transform of a stack of images. In Young's work, patches of 679 m x 679 m were used. However, position and size of the patches were not thoroughly discussed in this or other works on marine radars. As the algorithm relies on the Fourier transform, it is necessary for the observation window to meet the requirement of homogeneity. A marine radar collects images of 360° by rotating the antenna. Unlike SAR images, the projection between the waves and the radar beam varies with the azimuth position. In addition, there is a significant decay in received power over the range. For these two reasons, the imaging mechanism introduces inhomogeneity into the radar images. This phenomenon has been documented, e.g. Reichert (1994); Lund, Collins, Graber, Terrill and Herbers (2014) and led to the common practice of selecting a homogeneous patch in the direction of the main wave

energy (Barstow et al., 2005; Al-Habashneh et al., 2015). Fig. 1 illustrates a typical setup of the radar and the choice of the window. The azimuth beam defined by the position of ϕ, following the mathematical convention. The window position is determined by the averaging azimuth value over grid points in the window ($\overline{\phi}$). In the case of the standard window that is oriented towards the main wave direction $\overline{\phi} = \pi/2$, other windows are indicated and their relative position to the main wave direction is denoted $\Delta\Phi = \overline{\phi} - \pi/2$.

Furthermore, additional imaging mechanisms have to be considered when applying the SAR imaging knowledge to marine radars. Marine radars typically scan under grazing incidence conditions, which leads to the effect of shadowing (Seemann, Ziemer and Senet, 1997). Analogue to tilt modulation, shadowing is primarily a geometric effect, however it also depends on the polarization. While for some radars, pure geometric shadowing may be a good model under HH polarization, VV polarization is associated with more diffraction and a more complex shadowing mechanism. To account for the influence of shadowing, one-dimensional wavenumber spectra from radar images were adjusted so that their tail followed that of a co-registered buoy spectrum (Nieto Borge et al., 2004). Chapter 5.3 in (Barstow et al., 2005) summarizes the processing steps to retrieve wave spectra from radar measurements. In engineering practice, there was a tendency to use windows with a wider azimuthal coverage. Although this technique allows to capture wave energy from a wide range of directions, the weighting between the different directions are not correct. Furthermore, employing the Fourier transform requires homogeneous input, which is violated by the inhomogeneous effect of the imaging mechanism in large windows.

Directional wave spectra obtained with this transfer function work well for sea states with a strongly dominant wave direction. However, the azimuthal dependence that was already observed by Reichert (1994) has a strong effect when capturing directional seas. Windsea waves show a frequency dependent directional spreading that is lowest at the spectral peak and up to $\pm 30°$ around the peak wave direction for the high frequency tail of the spectrum (Mitsuyasu, Tasai, Suhara, Mizuno, Ohkusu, Honda and Rikiishi, 1975; Hasselmann, Dunckel and Ewing, 1980; Donelan, Drennan and Magnusson, 1996; Forristall and Ewans, 1998; Le Merle, Hauser, Peureux, Aouf, Schippers, Dufour and Dalphinet, 2021). The directional distribution reach up to $\pm 90°$, as found in measurements by high resolution Lidar (Lenain and Melville, 2017). All oblique waves are affected by a projection effect in radar images that leads to an underestimation of their energy contribution. This observation is well known in the radar community and has been empirically evaluated by Lund et al. (2014); Al-Habashneh et al. (2015). Although the imperfection of the MTF, especially for multimodal seas, has been noted (e.g. Lund et al. (2016)), an adjustment has not been proposed.

Herein, it will be demonstrated that the azimuthal dependency in the physical domain leads to a convolution in the spectral domain that is not easily invertible. The work presents an attempt to invert the convolution based on a simplifying assumption. The resulting tilt modulation transfer function is almost identical to the tilt MTF used for SAR images. The derivation provides new insight into how the position and size of the chosen window affects the estimated wave spectra, with a focus on the directional distribution of energy. The document is structured as follows: First, the theory of the 2d MTF is derived from geometric principles, ignoring the effect of shadowing (Sec. 2.1–(Sec. 2.5). The formula is then applied to measured (Sec. 2.7) and simulated radar images (Sec. 2.8). The results in Sec. 3 show that the proposed directional MTF is favorable in cases where the directional spreading is large. For the measured data spectra obtained by the suggested MTF leads to an energy distribution that is closer to that of a waverider buoy. In cases of high directional spreading the deviation between buoy and radar spectrum could be reduced by 17% with the 2d–MTF in comparison to the standard method. The same result was obtained with simulations where the retrieved directional spectrum was compared with the realization of the input wave spectrum.

The proposed method opens new possibilities for a more flexible application of the radar, in particular in coastal areas where windows of a more oblique angles can cover larger parts along the shoreline. Before the method can be adopted for operational usage it requires a thorough validation for a wide range of situations. The discussion in Sec. 4 serves as a first step to elaborate on the applicability and limitations of the 2d-MTF for various sea states. It further offers a qualitative investigation in the effect of the shadowing on the MTF. In the present form the method already shows considerable improvement of directional wave spectra imaged by marine radars.

2. Material and Methods

2.1. Formalism and assumptions

Fig. 2 shows an example radar image where all imaging effects are quite apparent: The strongest backscatter occurs close to the radar and and the portion of the waves that are most tilted towards the radar. In the regions where the radar beam and the wave crests are close to parallel, the backscatter from the gravity waves is reduced and dominated by

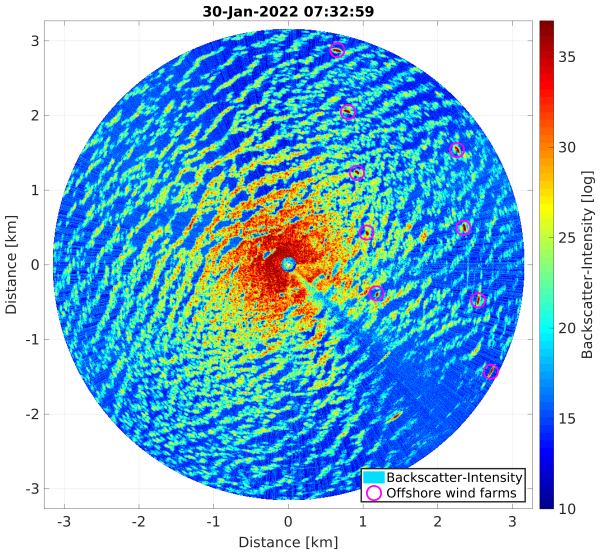

Figure 2: Example radar image from the FINO3 platform in the North sea. The image shows waves approaching the radar in the center of the image from the upper left. The waves are clearest at the azimuth angle where the radar beam faces the waves. If the radar beam and the wave crests are almost parallel the backscatter intensity decreases. Due to shadowing, the lowest backscatter intensities occur behind the waves. The shadowed areas increase in size with the distance from the radar.

smaller features that are directed towards the radar. With the distance from the radar, the shadowed areas increase and the intensity from the front face of the radar decreases as well.

According to the traditional MTF, the transformation from filtered image spectrum $\left|\mathcal{F}_{\mathrm{FiltImage}}\right|^2$ to wave spectrum $|\mathcal{F}\{\eta\}|^2$ only depends on the wavenumber k and two constants α, β.

$$|\mathcal{F}\{\eta\}|^2 = \frac{\alpha\,|\mathcal{F}\{\mathrm{FiltImage}\}|^2}{k^\beta} \tag{1}$$

α should be defined according to the radar calibration (compare Nieto-Borge, Hessner, Jarabo-Amores and De La Mata-Moya (2008)) and is not considered in this study. β depends on the properties of the radar that becomes mainly visible in terms of the shadowing. The Fourier operator $\mathcal{F}$ maps the time–space domain (t, x, y) to the frequency-wavenumber domain (ω, k_x, k_y). The standard MTF corrects the tilt modulation as a function of the wavenumber $k = \sqrt{k_x^2 + k_y^2}$. Hence the direction of the wave is not considered, and the MTF can therefore be regarded as one dimensional.

Herein, the derivation of the MTF is revisited in its general two-dimensional form, leading to an alternative formulation of the MTF, hereafter denoted directional MTF or 2d-MTF. The derived MTF disregards the definition of the constant α. The MTF used herein is an extension of the one-dimensional case, following the formalisms in Støle-Hentschel et al. (2018). Analogue to that study, the focus is on correcting the imaging mechanism of tilt modulation (Alpers, Ross and Rufenach, 1981; Wetzel, 1986). It is assumed that the analysis windows are selected close enough to the radar that shadowing only plays a minor role. Hence, shadowing effects are not taken into consideration and will have to be dealt with separately if they exist (Plant and Farquharson, 2012). An initial attempt on understanding the influence of the shadowing on the MTF will be provided in Sec. 4.

2.2. Relation between backscattering coefficients and local incidence angle

Under the assumption of the Bragg mechanism, the backscattering coefficient σ^0 for the different polarizations pp is

$$\sigma^0_{pp} = 4k_{\mathrm{EM}}^4 L^2 (\Delta h)^2 \cos^4(\theta_l) \left|f_{pp}(\theta)\right|^2 \exp\left(-k_{\mathrm{EM}}^2 L^2 \sin^2(\theta_l)\right), \tag{2}$$

where k_{EM} is the wave number of the electromagnetic wave, θ_l is the local incidence angle, ε_r the dielectric constant, Δh the height variation of the roughness and L the correlation length of the roughness of the observed surface (compare

Rees (2013), Eq. 3.51). The reflection coefficients for the Bragg backscattering mechanism at horizontal (HH) and vertical polarization (VV) are

$$f_{HH}(\theta_l) = \frac{\cos(\theta_l) - \sqrt{\varepsilon_r - \sin^2(\theta_l)}}{\cos(\theta_l) + \sqrt{\varepsilon_r - \sin^2(\theta_l)}}, \tag{3}$$

$$f_{VV}(\theta_l) = (\varepsilon_r - 1)\frac{\sin^2(\theta_l) - \varepsilon_r\left(1 + \sin^2(\theta_l)\right)}{\left(\varepsilon_r \cos(\theta_l) + \sqrt{\varepsilon_r - \sin^2(\theta_l)}\right)^2}, \tag{4}$$

Depending on the water temperature, the dielectric constant, is in the range of $[70; 80]$. Δh and L are assumed to be constant for a given sea state. Hence the backscattering coefficient varies predominantly with the local incidence angle.

For high grazing angles,

$$\left|f_{HH}\right| \approx 1 \tag{5}$$

and hence $\sigma^0_{HH} \propto \cos^4(\theta_l)$. For vertical polarization the local incidence angle changes the reflection coefficient. The above equation may be approximated by the following:

$$\left|f_{VV}\right| \approx \left|\frac{-1 - \sin^2(\theta_l)}{\cos(\theta_l)}\right| \tag{6}$$

leading to the backscattering coefficient

$$\sigma_0 \propto \begin{cases} \frac{\cos^4(\theta_l)}{r^4} & \text{for HH} \\ \frac{\cos^2(\theta_l)(-1-\sin^2(\theta_l))^2}{r^4} & \text{for VV} \end{cases} \tag{7}$$

The formulation for the vertical polarization complicates the inversion and thereby the definition of an MTF. Therefore, the following simplification was applied.

$$\sigma_0 \propto \begin{cases} \frac{\cos^4(\theta_l)}{r^4} & \text{for HH} \\ \frac{\cos^2(\theta_l)}{r^4} & \text{for VV} \end{cases} \tag{8}$$

Simulations have shown that this formulation for VV is a rough approximation, however, it is a necessary one. A general inversion of Eq. 14 is only possible based on simplifying assumptions.

2.3. Relation between local incidence angle and wave field

As shown in the previous section, the radar backscatter can be approximated as a function of the local angle of incidence which is related to the surface elevation of the waves as shown below. The origin of the coordinate system is defined at the horizontal position of the radar antenna with the vertical component at the mean water level. The horizontal coordinates x, y can also be expressed in polar coordinates $r = \sqrt{x^2 + y^2}, \phi = \arctan(y/x)$ in polar coordinates. The y-axis is oriented towards the directions where the waves are coming from (peak wave direction). Hence, the peak wave direction corresponds to $\phi = \pi/2$. Fig. 3 illustrates θ_l as the angle between the surface normal $\mathbf{n}$ and the backscatter vector $\mathbf{b}$ pointing form the surface to the radar antenna. The vectors are defined from the gradient of the surface elevation η and from the position of the observed point with respect to the radar antenna at the height H above the sea level (Støle-Hentschel et al., 2018)

$$\mathbf{n} = (-\partial\eta/\partial x, -\partial\eta/\partial y, 1), \tag{9}$$

$$\mathbf{b} = (-x, -y, H - \eta). \tag{10}$$

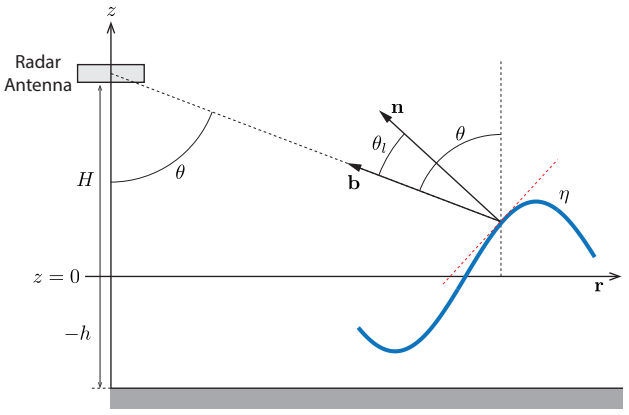

Figure 3: Illustration of local incidence angle θ_l depending on the range r, the antenna height H and the surface elevation η. Together, they define the vector pointing back to the radar antenna $\mathbf{b}$ and the surface normal $\mathbf{n}$. The water depth h is relevant for the dispersion filter.

The local incidence angle is thus given by

$$\mathbf{n} \cdot \mathbf{b} = |\mathbf{n}|\,|\mathbf{b}| \cos(\theta_l), \tag{11}$$

for every point in the radar image. The length of the vectors can be approximated,

$$|\mathbf{n}| = \sqrt{(\partial\eta/\,\partial x)^2 + (\partial\eta/\,\partial y)^2. + 1} \approx 1 \tag{12}$$

$$|\mathbf{b}| = \sqrt{r^2 + (H-\eta)^2} \approx r, \tag{13}$$

based on $(\partial\eta/\,\partial x)^2 \ll 1$, $(\partial\eta/\,\partial y)^2 \ll 1$ and $(H-\eta)^2 \ll r^2$. Here, we assume that the waves have a limited steepness and hence the square of there slopes is a small number. It is further assumed that the region of analysis has sufficient distance to the radar antenna such that $r \gg H$. Employing the above simplifications and replacing $x = r\cos(\phi)$ and $y = r\sin(\phi)$, Eq. 11 can then be approximated by

$$\cos(\theta_l) = \cos(\phi)\partial\eta/\partial x + \sin(\phi)\partial\eta/\partial y, \tag{14}$$

where it was assumed that $\frac{H-\eta}{r} \ll 1$.

Analogue to Støle-Hentschel et al. (2018), the last term on the left hand side is neglected and hence the term $\cos(\theta_l)$ results from a pure geometric description.

2.4. Wave inversion of unidirectional waves

Whenever it can be assumed that the waves are approximately unidirectional (with $\partial\eta/\partial x \approx 0$), Eq. 14, the tilt of the waves is easily retrieved

$$\partial\eta/\partial y = \frac{\cos(\theta_l)}{\sin(\phi)} \tag{15}$$

The surface elevation can be found by numerical integration in the physical domain or in the wavenumber domain.

2.5. Wave inversion of directional waves

For the case of directional seas, the surface elevation is retrieved by applying the Fourier transform $\mathcal{F}$ to Eq. 14. As the input data is a three-dimensional data stack for a given window in space and time, the employed Fourier transform is three-dimensional.

$$\begin{aligned}&\mathcal{F}\left(\cos(\theta_l)\right) \approx \\ &\mathcal{F}\left[\cos(\phi)\right] * \left[\mathrm{i}k_x\mathcal{F}(\eta)\right] + \mathcal{F}\left[\sin(\phi)\right] * \left[\mathrm{i}k_y\mathcal{F}(\eta)\right].\end{aligned} \tag{16}$$

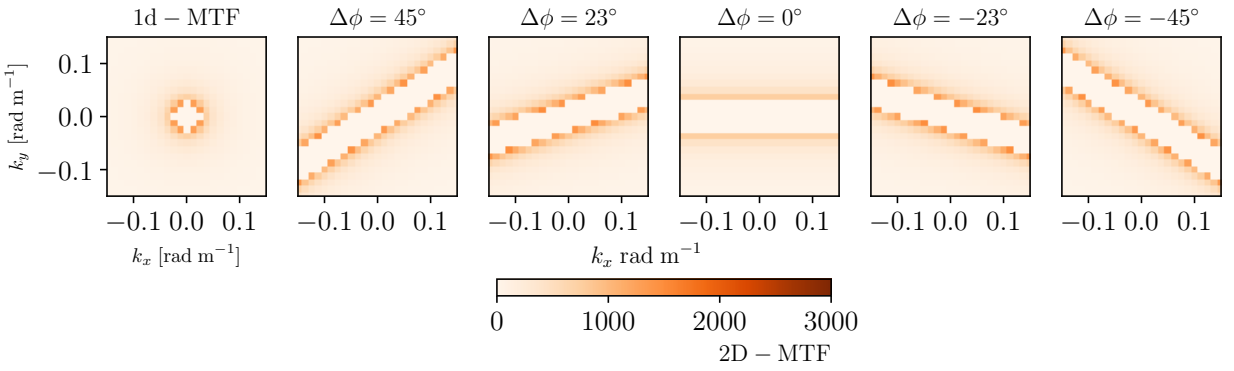

Figure 4: Comparison of 1–d MTF (left) with 2–d MTFs for different window positions. The angle $\Delta\phi$ denotes the angle between the standard window in the peak wave direction and the given window. To avoid artificial amplification of noise, MTF values exceeding a certain threshold are set to zero. For the 1d–MTF the omitted area has a circular shape while for the 2d–MTF it is a bar oriented according to $\Delta\phi$.

Inverting the latter equation would require a deconvolution, which can only be accomplished approximately and at a rather high computational cost (see for example Støle-Hentschel, Borge and Trulsen (2021)). Instead, the convolution operators are replaced by the multiplication with constants. Numerically, the convolution is a matrix multiplication where the convolution matrix (CM) is a diagonal matrix. In the present case, the input vector is the Fourier transform of $\cos(\phi)$ or $\sin(\phi)$. The convolution matrix is formed such that the zeroth Fourier component is on the main diagonal and the remaining components on the sub–diagonals. Denoting the i-th component of the Fourier transform as $\mathcal{F}_i$, the convolution matrix has the following form

$$\mathrm{CM} = \begin{bmatrix} \mathcal{F}_0 & \mathcal{F}_{-1} & \mathcal{F}_{-2} & \\ \mathcal{F}_1 & \mathcal{F}_0 & \mathcal{F}_{-1} & \\ & \ddots & \ddots & \\ & \mathcal{F}_2 & \mathcal{F}_1 & \mathcal{F}_0 \end{bmatrix} \tag{17}$$

If the window of observation is sufficiently small, ϕ changes little and so it can be assumed that $\cos(\phi)$ and $\sin(\phi)$ are almost constant within the window. In the spectral domain, this corresponds to the zeroth component, i.e. the main diagonal, being dominant.

$$\mathcal{F}_0 \gg \sum_{i\neq 0} |\mathcal{F}_i|, \tag{18}$$

and the Fourier coefficients for $i \neq 1$ can be set to zero

$$\mathrm{CM} \approx \begin{bmatrix} \mathcal{F}_0 & 0 & 0 & \\ 0 & \mathcal{F}_0 & 0 & \\ & \ddots & \ddots & \\ & 0 & 0 & \mathcal{F}_0 \end{bmatrix} = \mathcal{F}_0 \begin{bmatrix} 1 & 0 & 0 & \\ 0 & 1 & 0 & \\ & \ddots & \ddots & \\ & 0 & 0 & 1 \end{bmatrix} \tag{19}$$

By neglecting the sidebands of the matrix, the convolution matrix can be reduced to a multiplication by the product of zeroth Fourier coefficient, that represents the mean values of the respective input functions calculated over all the grid points within the window.

$$\mathcal{F}_0[\cos(\phi)] = \overline{\cos(\phi)} \tag{20}$$

$$\mathcal{F}_0[\sin(\phi)] = \overline{\sin(\phi)}. \tag{21}$$

With this simplification of Eq. 16, it can be inverted, yielding the directional MTF

$$\mathcal{F}(\eta) \approx \frac{\mathcal{F}\left(\cos(\theta_l)\right)}{\mathrm{i}\left(k_x\overline{\cos(\phi)} + k_y\overline{\sin(\phi)}\right)}. \tag{22}$$

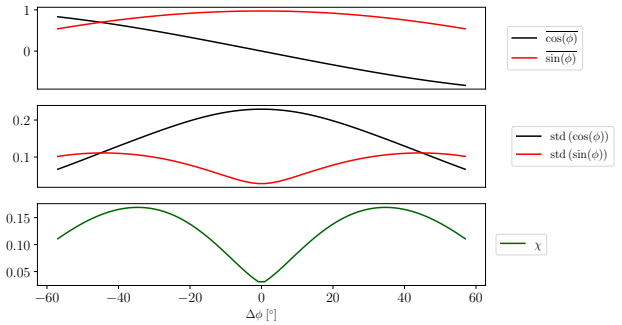

Figure 5: Example of $\overline{\cos(\phi)}$ and $\overline{\sin(\phi)}$, the standard deviation for $\cos(\phi)$ and $\sin(\phi)$ and the resulting projection variation indicator χ, the associated confidence measure is defined by $1-\chi$. For a confidence close to 1, the 2d MTF is well suited to invert the tilt modulation for the given window, while a low confidence implies that the directional energy distribution has a strong bias towards the mean direction. In the presented example, all windows cover the vertical width of $y \in [200\text{m}; 700\text{m}]$ and horizontal width of 500m. The angle $\Delta\phi = \overline{\phi} - \pi/2$ denotes the window position with respect to the standard window in the main wave direction.

Upon reformulation of this MTF it can be shown that is almost identical to the MTF used in the SAR community. The wavenumber components are transferred to polar coordinates, $k_x = \cos(\phi)k$ and $k_y = \sin(\phi)k$.

$$k_x\overline{\cos(\phi)} + k_y\overline{\sin(\phi)} = k\left(\cos(\phi)\overline{\cos(\phi)} + \sin(\phi)\overline{\sin(\phi)}\right) \approx k\cos\left(\phi - \overline{\phi}\right) \tag{23}$$

The approximation results from assuming that $\overline{\cos(\phi)} \approx \cos(\overline{\phi})$. For the two formulations to be identical $\overline{\cos(\phi)}$ must be equal to $\cos(\overline{\phi})$ and $\overline{\sin(\phi)}$ must be equal to $\sin(\overline{\phi})$.

Examples of the directional MTF for different window positions are shown in Fig.4(b–d). The average angle within the chosen window is defined $\overline{\phi}$. The standard window is defined symmetrically around the y-axis when the main wave direction is aligned with the y-axis and the waves are propagating against the direction of the axis. In this case $\overline{\phi} = \pi/2$ (as illustrated in Fig 1). To see how deviating the window position from the standard position, we define the angle $\Delta\phi = \bar{\phi} - \pi/2$. The standard 1d-MTF is added for comparison (see Fig.4a). When the denominator of the MTF tends towards zero the MTF would result in extreme amplifications that must be suppressed. In the 1d-MTF this leads to a circular filter around the origin of the (k_x, k_y) plane. For the 2d-MTF, filtering the denominator results in a bar tilted such that the bar forms an angle of $\Delta\phi$ with respect to the positive x-axis.

The underlying assumption that the window is small enough to omit the non-zero Fourier coefficients in the convolutions induces an error. The impact of this error can be quantified by analyzing the standard deviations of the projection factors for all grid points in the window, std(cos(ϕ)), std(sin(ϕ)). The confidence measure is finalized by weighting the respective standard deviations with their actual value. It is denoted the projection variation indicator (χ) and only depends on the position and size of a given observation window.

$$\chi = \left|\text{std}\left[\cos(\phi)\right]\overline{\cos(\phi)}\right| + \left|\text{std}\left[\sin(\phi)\right]\overline{\sin(\phi)}\right|. \tag{24}$$

Fig. 5 shows the projection variation indicator based on the contributing components for different window positions. χ must lie in the interval $[0; 1]$, $\chi = 0$ meaning that the radar beams are indeed parallel and $\chi = 1$ occurs for the full 360° image. One can approximate $\chi = 0$ by defining the observation window in the far range which was so far excluded due to shadowing. The confidence of the 2d MTF can be defined as $1 - \chi$, i. e. when the beams are parallel the confidence in the modulation transfer function is high ($1 - \chi \to 1$) and when the beams cover a wide range of azimuthal angles, the confidence is low ($1 - \chi \to 0$). It is emphasized that a high confidence reflects how well the MTF is suited to invert the azimuth convolution. However, a high confidence also implies that the window restricts the directionality that can be observed by the radar due to very low SNR at extreme angles between the radar beam and the wave direction.

The presented theoretical considerations highlight the general challenge when working with marine radars: The azimuth convolution intermingles information available in the physical domain (projection coefficient depending on

the position) and information available in the spectral domain (the wave direction of a given spectral component). Based on the theoretical analysis it can be concluded that the two-dimensional MTF approximates a correction of the tilt modulation and the azimuth convolution. The quality of the correction depends on both, the directional distribution of power spectral density, and on the choice of the window position and size.

2.6. Definition of estimated wave spectra

The core of the paper is to compare the directional wave spectra obtained by the 1d–MTF $F_{1d}(k_x, k_y)$ with that from the 2d–MTF $F_{2d}(k_x, k_y)$,

$$F_{1d}(k_x, k_y) = \frac{\widetilde{F}_{1d}(k_x, k_y)}{\int_{k_0}^{k_1}\int_{k_0}^{k_1}\widetilde{F}_{1d}dkxdky}, \tag{25}$$

$$F_{2d}(k_x, k_y) = \frac{\widetilde{F}_{2d}(k_x, k_y)}{\int_{k_0}^{k_1}\int_{k_0}^{k_1}\widetilde{F}_{2d}(k_x, k_y)dkxdky}, \tag{26}$$

The scaling by the energy in the interval $[k_0, k_1]x[k_0, k_1]$ with $k_0 = 0.025$ rad m^{-1} and $k_1 = 0.14$ rad m^{-1} simplifies the comparison with reference data. The unscaled wavenumber spectra $\widetilde{F}_{1d}(k_x, k_y)$ and $\widetilde{F}_{1d}(k_x, k_y)$ are defined as the product of the image spectrum $\mathcal{F}_{\mathrm{FiltImage}}$ and the respective MTFs $(\mathcal{T}_{1d})$ and $(\mathcal{T}_{2d})$:

$$\widetilde{F}_{1d}(k_x, k_y) = \mathcal{T}_{1d} \times F_{\mathrm{FiltImage}}, \tag{27}$$

$$\widetilde{F}_{2d}(k_x, k_y) = \mathcal{T}_{2d} \times F_{\mathrm{FiltImage}}, \tag{28}$$

where,

$$\mathcal{T}_{1d} = \frac{\alpha}{k^2}, \tag{29}$$

$$\mathcal{T}_{2d} = \frac{\alpha}{\left(k_x\overline{\cos(\phi)} + k_y\overline{\sin(\phi)}\right)^2}, \tag{30}$$

Both MTFs depend on the value of α, a unique factor for the analysis of all cases but differs between measurements ($\alpha = 1.2$) and simulation ($\alpha = 1$).

For comparison to the wavenumber spectra based on radar images, the directional spectra ($F(k_x, k_y)$) were also converted to frequency spectra.

$$S(f) = \int_0^{2\pi} F^*(k, \theta)\frac{dk(f)}{df}d\theta, \tag{31}$$

$$F^*(k, \theta) = F(k_x, k_y)k \tag{32}$$

The deviation between reference spectrum and obtained spectrum is evaluated by the overall error

$$\epsilon_{1\mathrm{d},2\mathrm{d}} = \sum \left|F_{1\mathrm{d},2\mathrm{d}} - F_{\mathrm{Reference}}\right| \tag{33}$$

$$\epsilon = \sum S(f) - S_{\mathrm{Reference}}(f) \tag{34}$$

The measured and simulated sea states are summarized in Table 1. The reference spectra for the measurements were retrieved from the buoy by applying the maximum likelyhood method (EMEM) where the spreading is not implicitly given as a parameter. For the simulation the wave spectra were calculated from JONSWAP spectra with the directional distribution based on the approach by Mitsuyasu et al. (1975). The directional distribution involves three parameters: s_{max} (whose value increases as the directional dispersion decreases), μ_1 and μ_2. In these simulations, the typical values $\mu 1 = 5$ and $\mu 2 = -2.5$ have been used.

Table 1
Available parameters of the sea states for the measured and simulation examples.

Case	H_s [m]	T_p [s]	Directional Spreading	γ
M1	3.9	7.0	high	–
M2	7.6	10.9	low	–
S1	1.9	6.3	high, $s_{\max}$=15	5.2
S2	1.9	6.3	moderate, $s_{\max}$=45	5.2

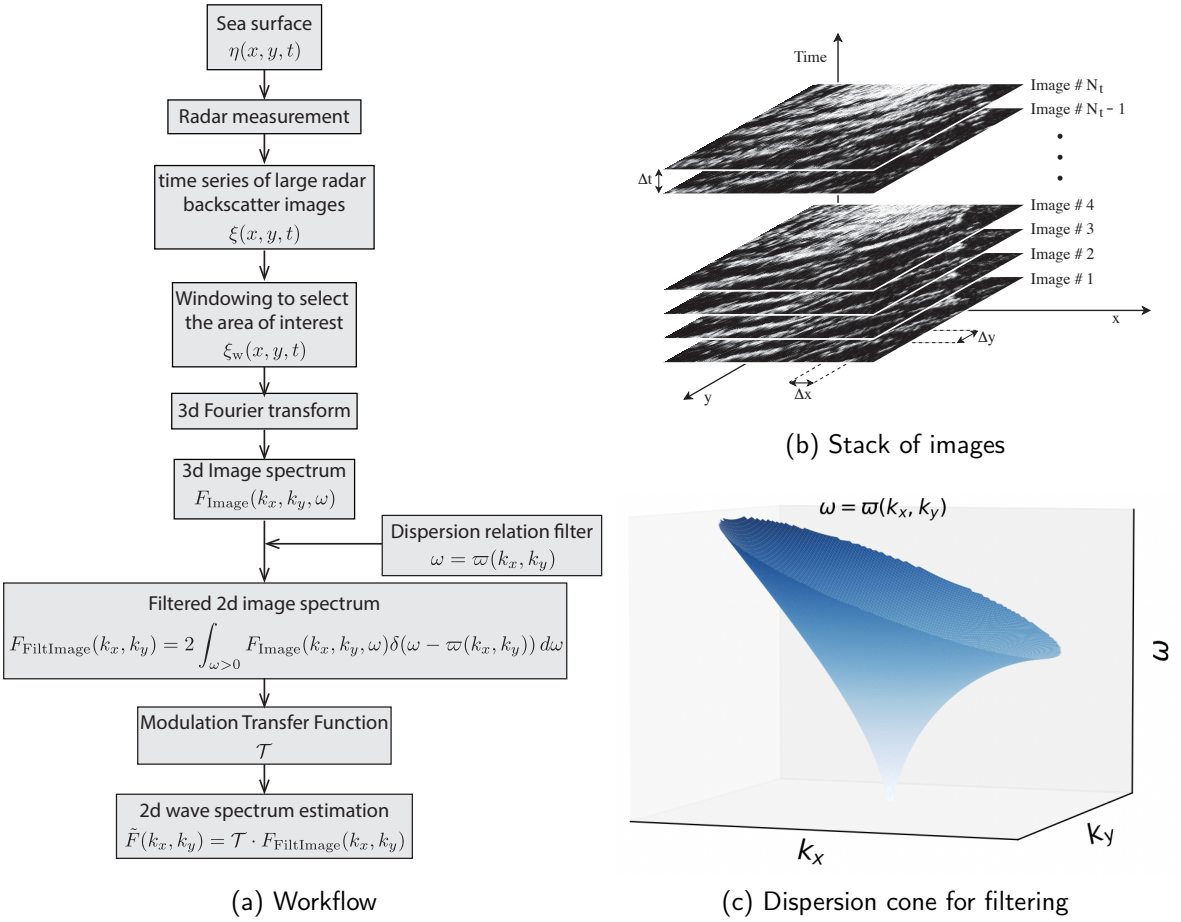

(a) Workflow

(b) Stack of images

(c) Dispersion cone for filtering

Figure 6: Summary of the workflow (a), illustration of the stack of radar images used that is selected for the 3d Fourier transform (b) and the dispersion filter illustrated in (c), where the assymmetric shape results from the influence of the current.

2.7. Application to measured data

The radar data utilized in this study were acquired by Hereon's coherent on receive marine X-band (9.4 GHz) radar (Horstmann, Bödewadt, Carrasco, Cysewski, Seemann and Stresser, 2021). The radar was mounted at 43 m height, on the offshore platform FINO-3, located 80 km west of Sylt (North Sea). The radar covers a range of 3150 m, where the water depth is around 23 m. The radar antenna rotates approximately at 30 rpm, two seconds per rotation. The pulse repetition frequency was set to 2 kHz, where the radar range data was acquired at 20 MHz, therefore the range sampling resolution was 7.5 m. The transmitted pulse length was approximately 65 ns, so the effective range resolution should be around 9.75 m. The antenna angular resolution was 1.2° with vertical polarization.

The processing from the raw images to the directional spectrum is illustrated in Fig. 6 and outlined below and follows the standard procedure (e.g. described by Young et al. (1985); Nieto-Borge, Reichert and Dittmer (1999);

Senet, Seemann and Ziemer (2001); Nieto Borge et al. (2004); Nieto-Borge et al. (2008); Ziemer and Günther (1994); Ziemer and Dittmer (1994)).

1. Select 128 radar backscatter intensity images (range,azimuth) (see illustration of stack of radar images in Fig. 6b). Retrieve surface currents (Ux,Uy) and main wave direction.
2. Retrieve data correspondent to desired window coordinates applying linear interpolation.
3. Overall scaling: All windows are scaled by a common factor that approximates a normalization of the uncalibrated radar return.
4. Retrieve wavenumber spectrum: Retrieve 3D spectra (k_x,k_y,ω) from the analysis window, then locate the energy around the dispersion relation (see illustration of the dispersion filter in Fig. 6c), taking in account the currents and finally integrate the energy in frequency domain.
5. Highpass filtering on 2d-spectra eliminating power spectral density for $k < 0.38$ rad s^{-1}.
6. Apply the MTF (Eq. 27 or Eq. 28)
7. Energy-dependent scaling: Division by $\int_{k_0}^{k_1}\int_{k_0}^{k_1} F(k_x,k_y)dk_x dk_y$, where $k_0 = 0.05$ rad m^{-1} and $k_1 = 1.4$ rad s^{-1}(Eq. 25 or Eq. 26)
8. Interpolate obtained (k_x, k_y)-spectra to achieve matching grid with 2d buoy spectrum
9. Transformation of the 2d-spectra to polar coordinates and integration over the angle (Eq. 31 and Eq. 32).

2.8. Application to simulated radar images

The algorithm is further applied to synthesized radar images based on the surface elevation maps of linearly simulated ocean waves. The employed simulation algorithm has been described in Nieto Borge et al. (2004) for HH polarization. Herein, the simulations were altered from HH to VV replacing the incidence dependency for HH, $\cos^4(\theta_l)$, by that for VV $\cos^2(\theta_l)\left(-1-\sin^2(\theta_l)\right)^2$ (compare 7).

The wave fields were based on directional JONSWAP spectra. The spectral parameters for the simulated cases are summarized in Table 1 and include seas with different peak periods (T_p), significant wave height (H_s), spectral enhancement factor (γ) and directional spreading ($s_{\max}$).

The steps of the simulation are summarized briefly below.

- Definition of a directional JONSWAP spectrum based on the provided parameters (compare Table 1).
- Generation of linearly propagating surface waves based on the directional wave spectrum (resolution $\delta X = \delta Y =$ 7.5m, δ2s, Simulation Time 256 s)
- The radar imaging was simulated for the generated surface waves by calculating the local angle of incidence measured from the sea surface facet projection in the direction of the radar antenna (Støle-Hentschel et al., 2018). Shadowed areas are treated by the geometric shadowing approach. The SPM electromagnetic scattering model Rees (2013) is employed to estimate the normalized radar cross section (NRCS). Finally, the radar equation is applied to the NRCS estimation (see Eq. 2).
- selection of observation windows with a side length of 480m

The processing of the data is performed as described above, analogue to the measured data.

3. Results

3.1. Comparison of wave spectra measured by radar and buoy

Fig. 7 and 8 highlight how the two MTFs transform the image spectra into different wavenumber spectra. The cases are summarized as M1 and M2 in Tab. 1. M1 has a clearly higher directional spreading. The energy distribution in the image spectra changes with the analysis window. Two other sea states were analyzed but are omitted here as they provide no additional value. The analysis of the measured sea states has shown that the power spectral density of the filtered image spectrum is amplified for wavenumber vectors aligned with the mean radar beam position and diminished for wavenumber vectors oblique to the mean radar beam position (compare Lund et al. (2016)). This effect is only corrected by the 2d MTF. The applicability is however limited by the bar inherently present in the 2d MTF (compare $\Delta\phi = -45°$

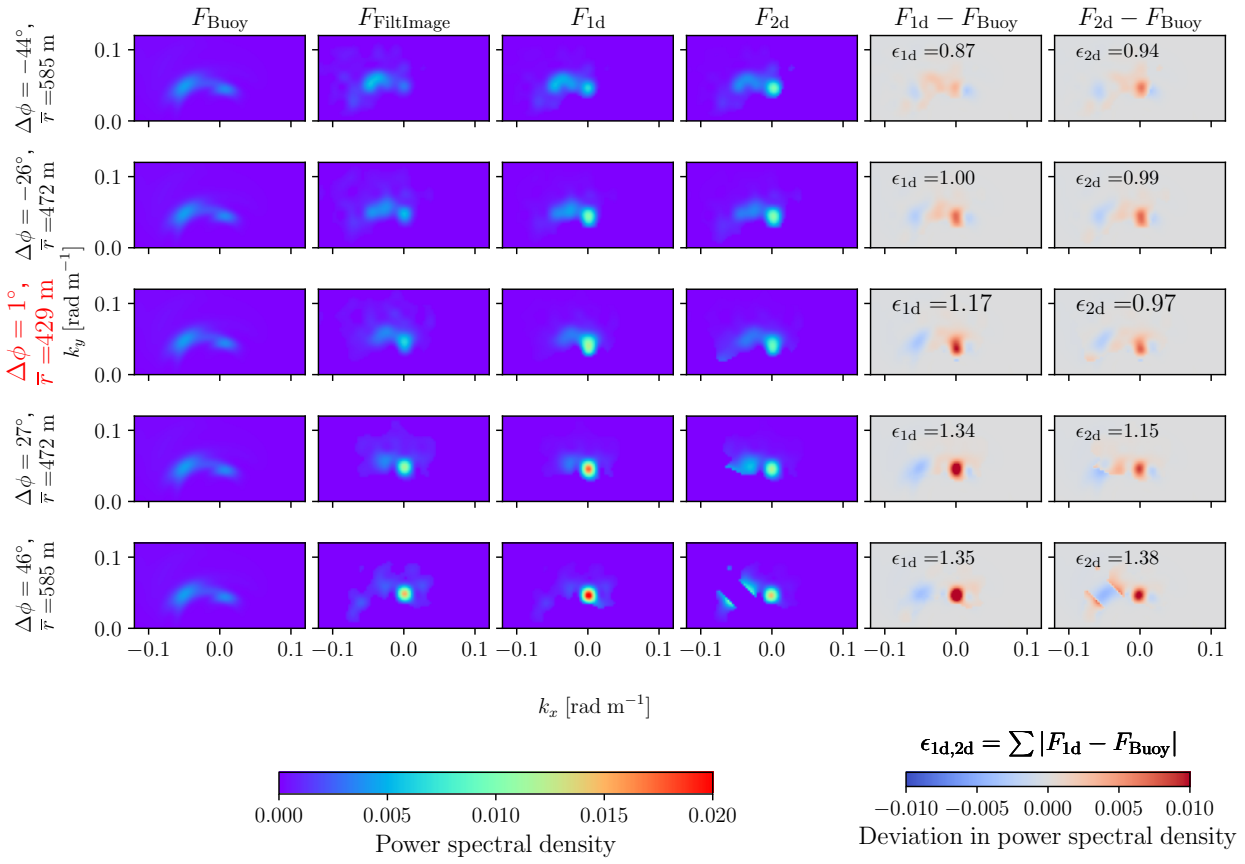

Figure 7: Measured wavenumber (k_x, k_y) spectra for a sea state M1 (Tab. 1), based on different data sources, from left to right:Buoy (F_{buoy}), Filtered image spectrum (F_{image}), Filtered image spectrum with 1d-MTF applied ($F_{1\mathrm{d}}$), filtered image spectrum with 2d-MTF applied ($F_{2\mathrm{d}}$). The right most columns show the deviation between radar spectra and the buoy spectrum. For the radar images, each row is based on a different window position denoted by the corresponding relative angle to the standard position, $\Delta\phi$, and the average range value within the window, $\bar{(r)}$. The overall error for the given window is defined as $\epsilon_{1\mathrm{d,2d}} = \sum |F_{1\mathrm{d,2d}} - F_{\mathrm{Reference}}|$.

in Fig. 7). In cases where the wave energy is practically unidirectional, there is very little difference in the effect of the two MTFs. Furthermore, low wave numbers are not well captured by both methods.

For comparison, the buoy spectrum is shown and the difference between the two is calculated. As noted in the introduction, the directional spectrum from the buoy is known to be erroneous and cannot be regarded as ground truth. In the absence of the ground truth the method will be tested on simulated radar images where the wavenumber spectrum is known (see Sec. 2.8). After integrating the directional spectrum and obtaining the 1d frequency spectra, $S(f)$, the differences between the two methods are less apparent (see Fig. 9). Hence, the difference between the MTFs is really the directional distribution while the frequency distribution remains untouched. For the case M2, the lower frequency contributions of the spectrum are missing, leading to an overestimation of the higher frequencies due to the energy scaling. It appears that the radar is not able to retrieve energy below frequencies of 0.06 Hz for the given window size. The observed lower frequency limit is higher than assumed when requiring that wave lengths of half the window size would be recovered. For a window size of 500 m this corresponds to wavelengths of 0.0251 rad/m. For the given water depth at FINO3 of 23 m, the resulting theoretical lower frequency limit is 0.057 Hz. The upper limit is 0.27 Hz.

3.2. Comparison of wave spectra from simulated radar images to ground truth

Two examples of the retrieved wave spectra from simulated radar images are shown in Fig. 10 and Fig. 11. Their parameters are summarized as S1 and S2 in Tab. 1. The two cases only differ in the value of the directional spreading.

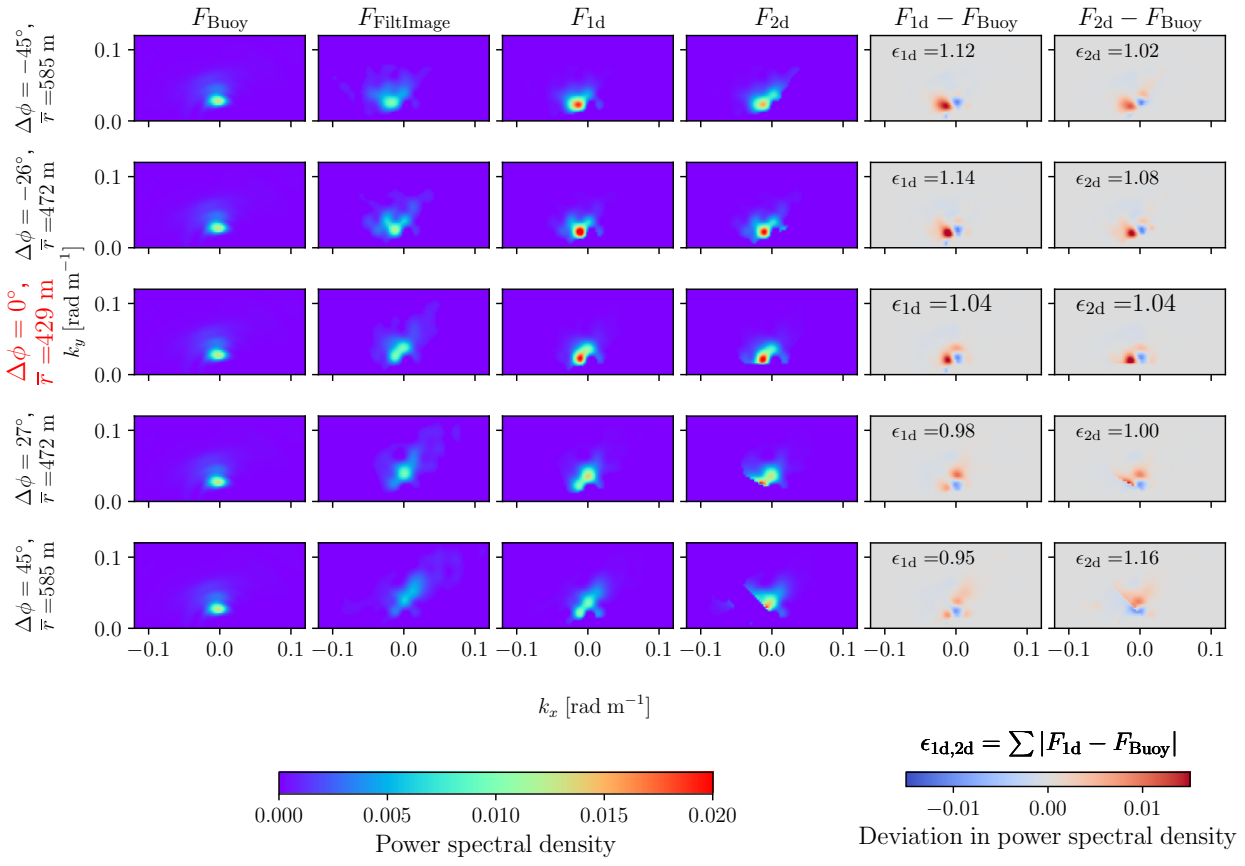

Figure 8: Measured wavenumber (k_x, k_y) spectra for a sea state M1 (Tab. 1), based on different data sources, from left to right: Buoy (F_{buoy}), Filtered image spectrum (F_{image}), Filtered image spectrum with 1d-MTF applied ($F_{1\mathrm{d}}$), filtered image spectrum with 2d-MTF applied ($F_{2\mathrm{d}}$). The right most columns show the deviation between radar spectra and the buoy spectrum. For the radar images, each row is based on a different window position denoted by the corresponding relative angle to the standard position, $\Delta\phi$, and the average range value within the window, $\bar{(r)}$. The overall error for the given window is defined as $\epsilon_{1\mathrm{d,2d}} = \sum |F_{1\mathrm{d,2d}} - F_{\mathrm{Reference}}|$.

The retrieved directional wave spectra for those cases are clearly better when the 2d-MTF has been applied. With the 1d-MTF the energy close to the k_y is artificially amplified. It is also noteworthy that the wave spectra differ for every window position.

Fig. 12 shows the frequency spectra for the simulated cases S1 and S2 in Table 1. When integrated over the directions, the differences between the two MTFs are no longer that apparent.

4. Discussion

4.1. Implications of the underlying assumptions and further development

This study shows that extending the MTF from a 1d to 2d tilt correction can help to better account for oblique waves in directional seas. These results require however that the window of analysis is small so that it may be assumed that the radar beams are roughly parallel within the window. The findings further reveal that employing an MTF to the entire radar image of 360° is problematic. The possibility of correcting the projection effect opens new possibilities in placing the observation window outside the main wave direction. This option will have to be further investigated in the future.

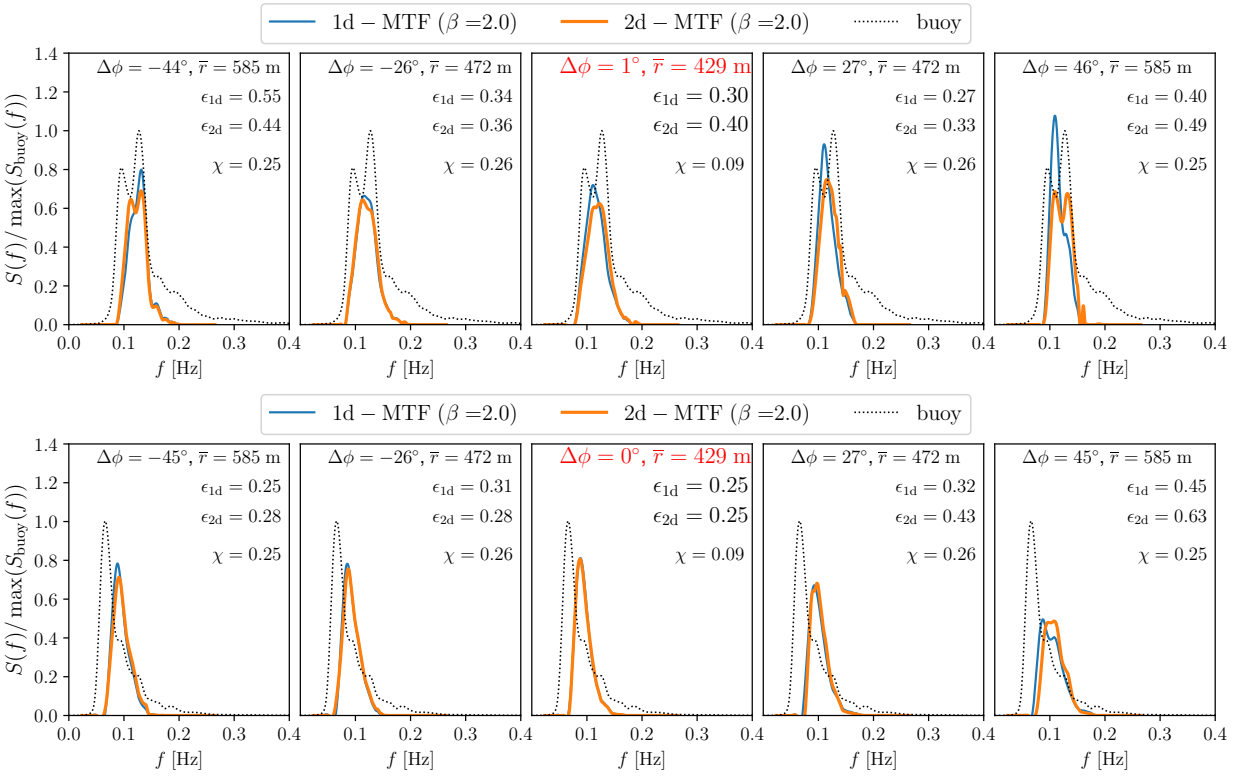

Figure 9: Frequency spectra based on different windows in the radar image for two sea states. Sea state 1 in the upper row and sea state 2 in the lower row. The indicated points average angles (θ) and average ranges ($\bar{r}$) indicate the position of the window.

It is well known that the directional spectra obtained from buoys are not capturing nature well (see introduction). Models to describe the directionality of sea states show different characteristics depending on the employed measurement instrument (Lenain and Melville, 2017; Paláez-Zapata, Pakrashi and Frédéric, 2023) and ground truth to evaluate obtained spectra are absent. In this study, simulations were employed in order to mitigate this shortcoming. Although both the model for the directional spreading of wave energy and the imaging mechanism of the radar may be questioned, it provides the only mean to properly validate the results. The simulations witness the effect of sampling variability in the sea surface. Since the observation time is too short, the estimation of the wave spectrum is different for every window within a given realization. Comparing the wave spectrum with that of a buoy is therefore questionable. Despite of the doubt if buoys are suitable in providing directional spectra, the measurements were obtained in a single position, not representative for each point in the radar footprint unless the observation time under stationary conditions would be much longer (Krogstad, Wolf, Thompson and Wyatt, 1999).

Applying the method requires some caution to avoid the amplification of noise. If the dot product between a wave number vector and the mean radar beam direction is small, the MTF will lead to an amplification of the obtained values. I.e., very long waves and waves perpendicular to the azimuth direction of the radar beam cannot be retrieved. As mentioned above, inverting the forward model of the imaging mechanism is a difficult problem. The assumption herein relies on a uniform correction that represents the average over the selected patch. To illustrate this two monochromatic waves and their respective azimuth dependent radar images are illustrated in Fig. 13. The simplification of the projection disregards the shown azimuthal variation in the images. The areas of low backscatter correspond to the areas where the inversion would lead to very large values and is therefore omitted. It is therefore important to compare the initial image spectrum, $\mathcal{F}_{\text{image}}$ and the MTF $\mathcal{T}_{2\text{d}}$ for the given window position as illustrated in Fig. 4. The bar of maximum amplification by the MTF should be located in a region in the kx-ky domain where the imaged waved energy is negligible.

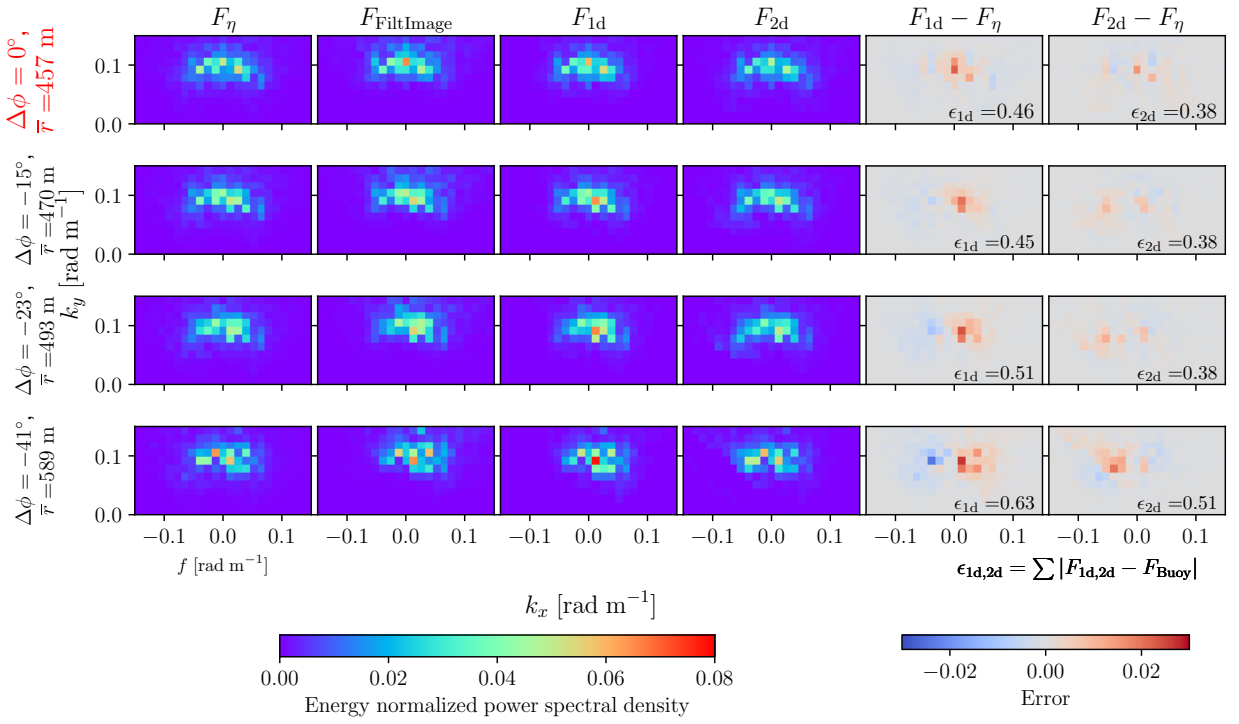

Figure 10: Simulated wavenumber (k_x, k_y) spectra for sea state S1 (Tab. 1), based on different data sources, from left to right: Wave spectrum $(\mathcal{F}_\eta)$, Filtered image spectrum $(\mathcal{F}_{\mathrm{image}})$, Filtered image spectrum with 1d-MTF applied $(\mathcal{F}_{1\mathrm{d}})$, filtered image spectrum with 2d-MTF applied $(\mathcal{F}_{2\mathrm{d}})$. The right most columns show the deviation between radar spectra and the buoy spectrum. For the radar images, each row is based on a different window position denoted by the corresponding relative angle to the standard position, $\Delta\phi$, and the average range value within the window, $(\bar{r})$. The overall error for the given window is defined as $\epsilon_{1\mathrm{d},2\mathrm{d}} = \sum |F_{1\mathrm{d},2\mathrm{d}} - F_{\mathrm{Reference}}|$.

4.2. Shadowing

This study was restricted to windows with minimal amount of shadowing. For completeness the influence of the shadowing on the MTF shall be assessed. Following Nieto Borge et al. (2004), it is assumed that the shadowing can be modeled as an illumination mask λ by which the surface elevation is multiplied:

$$\lambda = \begin{cases} 1 & \text{areas illuminated by the radar} \\ 0 & \text{shadowed areas, invisible to the radar} \end{cases} \tag{35}$$

Eq. 16 is reformulated replacing $\eta = \eta\lambda$

$$\begin{aligned} &\mathcal{F}\left[\cos(\phi)\right] * \left[\mathcal{F}\left(\frac{\partial \eta\lambda}{\partial x}\right)\right] + \mathcal{F}\left[\sin(\phi)\right] * \left[\mathcal{F}\left(\frac{\partial \eta\lambda}{\partial y}\right)\right] \\ &\approx \mathcal{F}\left(\cos(\theta_l)\right). \end{aligned} \tag{36}$$

the partial derivative for the x-direction becomes

$$\mathcal{F}\left(\frac{\partial \eta\lambda}{\partial x}\right) = \mathcal{F}(\lambda) * \left[\mathrm{i}k_x \mathcal{F}(\eta)\right] + \mathcal{F}\left(\eta\frac{\partial \lambda}{\partial x}\right) \tag{37}$$

and the equivalent for the y-direction. The convolution in the first term can be replaced by multiplication with a constant, owing to the domination of the zeroth component (compare Støle-Hentschel et al. (2021)). The second term contains the change of the MTF according to the degree of shadowing and will be studied in more detail here. In the absence of a valid and accurate shadowing model, geometric shadowing is assumed as first order approach. The derivative

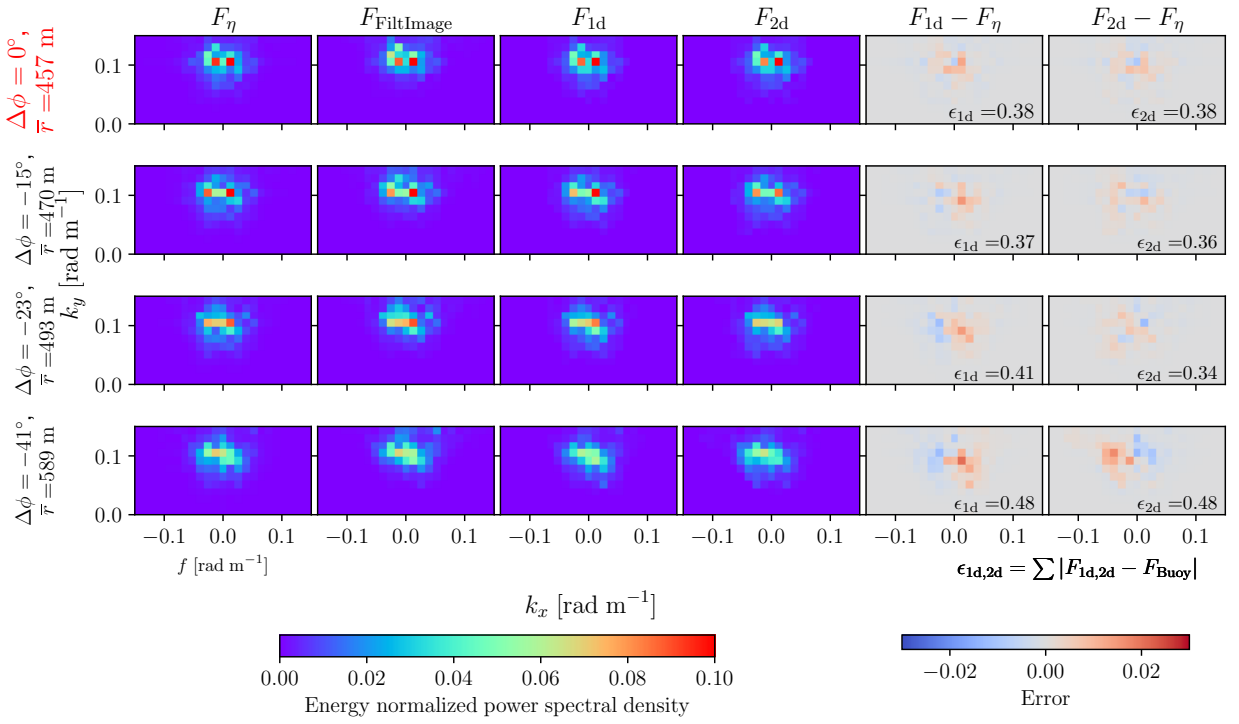

Figure 11: Simulated wavenumber (k_x, k_y) spectra for a sea state S1 (Tab. 1), based on different data sources, from left to right: Wave spectrum $(\mathcal{F}_\eta)$, Filtered image spectrum $(\mathcal{F}_{\text{image}})$, Filtered image spectrum with 1d-MTF applied $(\mathcal{F}_{1d})$, filtered image spectrum with 2d-MTF applied $(\mathcal{F}_{2d})$. The right most columns show the deviation between radar spectra and the buoy spectrum. For the radar images, each row is based on a different window position denoted by the corresponding relative angle to the standard position, $\Delta\phi$, and the average range value within the window, $(\bar{r})$. The overall error for the given window is defined as $\epsilon_{1d,2d} = \sum |F_{1d,2d} - F_{\text{Reference}}|$.

of the shadowing is only non-zero when the illumination function changes between shadowed and illuminated areas. The shadowing starts behind the peak and reaches towards some area between the following trough and the next peak. Hence the pattern depends highly on the sea state and the incidence angle. In reality, the radar characteristics are important to accurately describe the actual shadowing mechanism, e.g. the elevation of the antenna, the polarization, the pulse shape and the signal–to–noise ratio. For simplicity, it is assumed that the surface is either fully illuminated or fully shadowed (compare Fig. 14). Although the waves are generally irregular, statistically, it can be assumed that the shadows become longer with distance from the antenna. Below, we study the average affect by employing a simple sine wave with a given amplitude A. The shadowing is calculated with the ray tracing approach based on the antenna height H. The influence of A and H are compared by employing a running average on the MTF factor resulting from $\mathcal{F}\left(\eta \frac{\partial \lambda}{\partial x}\right)$. The results are shown in Fig. 15. It has been empirically derived for the 1d-MTF that the power law of the tilt modulation transfer function must be adapted. When applied to the power spectrum the 1d-MTF has the form

$$\frac{1}{k^\beta}; \quad \beta \in [1;2]. \tag{38}$$

As an example, Nieto Borge et al. (2004) has employed $\beta = 1.3$ based on swell dominated data. For pure tilt modulation $\beta = 2$. It has been assumed that the reduction of the β is related to shadowing. This assumption is confirmed with Fig. 15. Higher sea states and lower antenna heights are associated with more and longer shadows. These lead to a wave-number dependent addition of the MTF that balances some the tilt-modulation effects. It should further be noted that below the peak, the shadowing has the opposing effect and hence the adaption of β should be different before and behind the spectral peak.

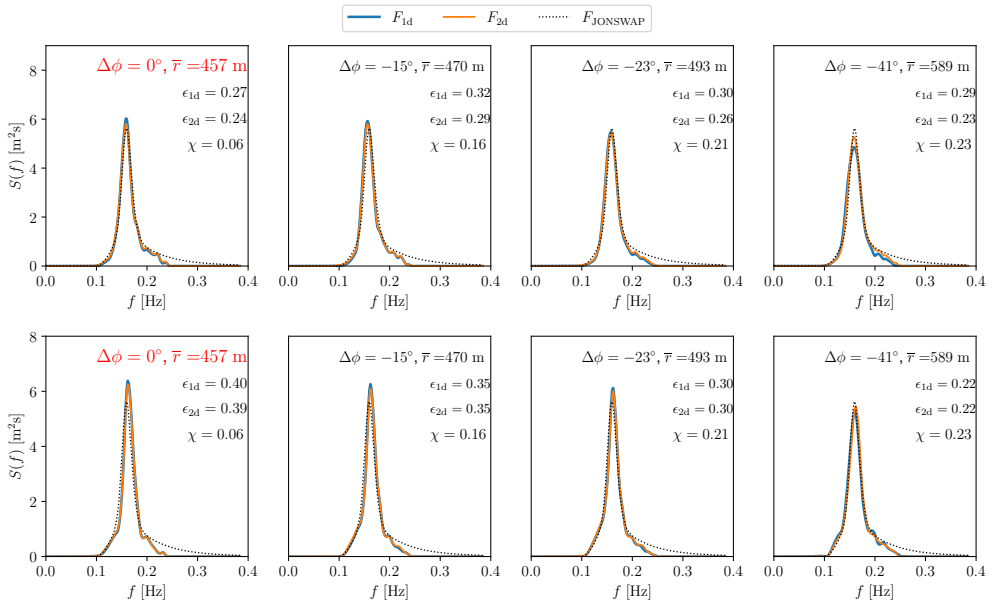

Figure 12: Reconstruction of 1D frequency spectra (cases 6-9) from simulated radar images based on the 1d–MTF and the 2d–MTF. For comparison the JONSWAP spectrum that was used for the wave simulations is plotted in black dots.

The formulation in Eq.37 reveals that the general from of the MTF in Eq. 38 is only a rough approximation. Following Eq. 36, the form of the MTF is given by

$$\mathcal{T}_{2d} = \frac{1}{\left(\overline{\cos(\phi)}k_x + c_1 k_x^{\beta_1} + \overline{\sin(\phi)}k_y + c_2 k_y^{\beta_2}\right)^2}, \tag{39}$$

with the constants $c_1, c_2, \beta_1, \beta_2$ depending on the window position and the nature of the shadowing that in turn depends on the sea state and the radar. The values can be estimated from simulations as illustrated in Fig. 15. For the used radar, the nature of the true shadowing is unknown but may be approximated. Incorporating the shadowing effect in a generalized MTF independent of the sea state conditions would go beyond the purpose of this study. Further improvements in retrieving wave spectra from marine radars requires an more profound understanding of the role of the shadowing in the MTF. Alternatively, removing the shadows (compare Støle-Hentschel et al. (2021)) may be an option to employ the full potential of the radar. Using the full radar image, including shadowed areas has a general merit. Not only does the shadowing imply a natural increase of the signal to noise ratio. When the distance to the radar is increased, observation windows of the same size include a smaller variation of direction, leading to a smaller value of the projection variation indicator χ. It is therefore expected that the directional MTF has good potential in the mid and far range.

5. Conclusion

Measurements and simulations demonstrate that the proposed directional MTF improves the directional wave spectra for cases where the spreading is high. This is shown by comparing the obtained wave spectra with those based on the state–of–the–art method. The latter tends to amplify the energy in the direction of the mean azimuth angle in the observation window. Depending on the position of the window, different wave directions are emphasized. This imbalance can be corrected by using the directional MTF (or 2d MTF). In addition to improving the estimation of directional sea states by marine radars, the proposed MTF provides more flexibility in the analysis of the images, e.g., to extend the area of coverage parallel to the beach. The choice of an appropriate analysis window also depends on the directional energy distribution. All wave components forming an angle of up to $\pm 45°$ with the radar beam are considered well captured. In order to cover all the relevant wave components, also in the case of multi-model seas, it

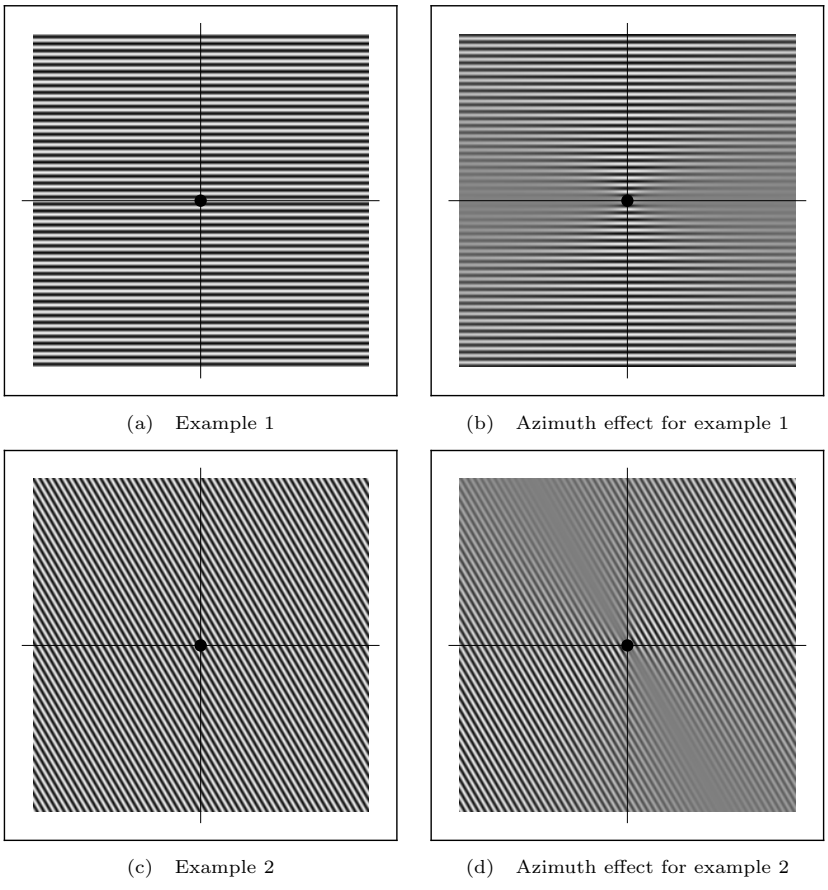

(a) Example 1 (b) Azimuth effect for example 1

(c) Example 2 (d) Azimuth effect for example 2

Figure 13: Illustration of monocromatic wave components with different wavelength and propagation direction (a and c) and the azimuth effect in their respective radar images (b and d). The antenna position is indicated by the black dot. All available MTFs treat the image as shown in a and c disregarding the azimuth dependent scaling shown in b and d. The 2d MTF ensures that the direction of the wave is taken into account, i.e. a and c are weighted differently.

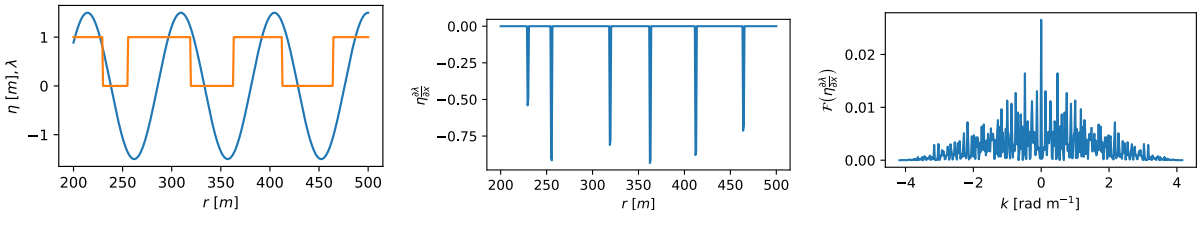

Figure 14: Left: η, λ, Middle: $\eta\frac{\partial\lambda}{\partial x}$, Right:$\mathcal{F}\left(\eta\frac{\partial\lambda}{\partial x}\right)$

is suggested to compose the directional wave spectrum based on multiple small windows, each dedicated to resolve a particular range of directional wave energy.

6. Acknowledgements

This work was funded by Minerva Fund and European Research Council through the HIGHWAVE project (grant no. 833125).

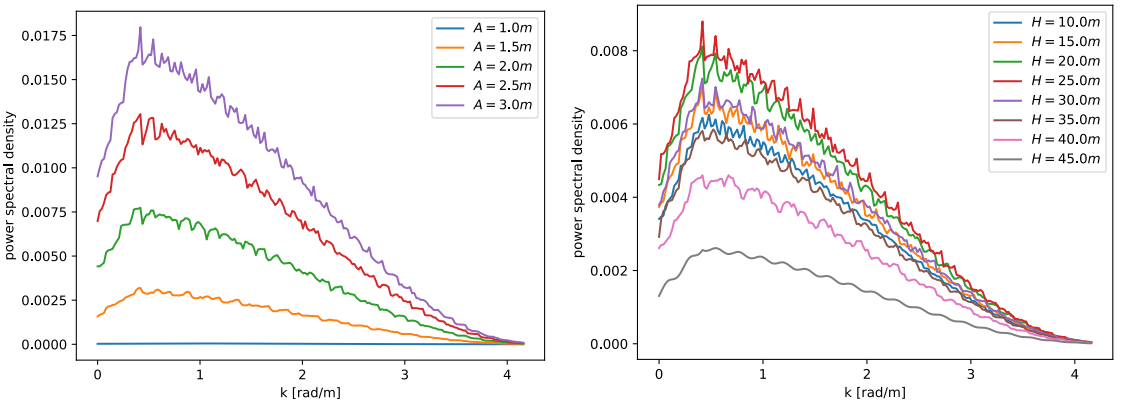

Figure 15: Influence of wave amplitude and incidence angle (radar height) for the shadowing related MTF addition. For low wave amplitudes and high radar antennas (with a resulting larger grazing angle), the deviation from the pure tilt modulation is minimal.

These data were collected and made freely available by the BSH marine environmental monitoring network (MARNET), the RAVE project (www.rave-offshore.de), the FINO project (www.fino-offshore.de) and cooperation partners of the BSH. The sea state portal was realized by the RAVE project (Research at alpha ventus), which was funded by the Federal Ministry for Economic Affairs and Climate Action on the basis of a resolution of the German Bundestag. This research was partially funded by the German-Israeli cooperation in Marine Sciences (BMBF-MOST), grant No. 3-15249. This research was partially funded by German Federal Ministry for Economic Affairs and Energy (BMWi), grant No. 0325915G.

Device: Datawell Directional Waverider DWR-MkIII

References

Al-Habashneh, A.A., Moloney, C., Gill, E.W., Huang, W., 2015. An adaptive method of wave spectrum estimation using x-band nautical radar. Remote Sensing 7, 16537–16554. URL: https://www.mdpi.com/2072-4292/7/12/15851, doi:10.3390/rs71215851.

Alpers, W., Hasselmann, K., 1978. The two-frequency microwave technique for measuring ocean spectra from an airplane or satellite. Boundary Layer Meteorol. 13, 215–230.

Alpers, W.R., Ross, D.B., Rufenach, C.L., 1981. On the detectability of ocean surface waves by real and synthetic aperture radar. Journal of Geophysical Research: Oceans 86, 6481–6498.

Barstow, S.F., Bidlot, J.R., Caires, S., Donelan, M.A., Drennan, W.M., Dupuis, H., Graber, H.C., Green, J.J., Gronlie, O., Guérin, C., Gurgel, K.W., Günther, H., Hauser, D., Hayes, K., Hessner, K., Hoja, D., Icard, D., Kahma, K.K., Keller, W.C., Krogstad, H.E., Lefevre, J.M., Lehner, S., Magnusson, A.K., Monbaliu, J., Nieto Borge, J.C., Pettersson, H., Plant, W.J., Quentin, C.G., Reichert, K., Reistad, M., Rosenthal, W., Saetra, O., Schulz-Stellenfleth, J., Walsh, E.J., Weill, A., Wolf, J., Wright, C.W., Wyatt, L.R., 2005. Measuring and Analysing the directional spectrum of ocean waves. COST 714; EUR 21367, COST Office. URL: https://hal.science/hal-00529755.

Capon, J., Greenfield, R.J., Kolker, R.J., 1967. Multidimensional maximum-likelihood processing of a large aperture seismic array. Proceedings of the IEEE 55, 192–211.

Donelan, M.A., Drennan, W., Magnusson, A.K., 1996. Nonstationary analysis of the directional properties of propagating waves. Journal of Physical Oceanography 26, 1901–1914.

Forristall, G.Z., Ewans, K.C., 1998. Worldwide measurements of directional wave spreading. Journal of Atmospheric and oceanic technology 15, 440–469.

Hasselmann, D.E., Dunckel, M., Ewing, J., 1980. Directional wave spectra observed during jonswap 1973. Journal of physical oceanography 10, 1264–1280.

Horstmann, J., Bödewadt, J., Carrasco, R., Cysewski, M., Seemann, J., Stresser, M., 2021. A coherent on receive x-band marine radar for ocean observations. Sensors 21. doi:10.3390/s21237828.

Krogstad, H.E., Wolf, J., Thompson, S.P., Wyatt, L.R., 1999. Methods for intercomparison of wave measurements. Coastal Engineering 37, 235–257.

Le Merle, E., Hauser, D., Peureux, C., Aouf, L., Schippers, P., Dufour, C., Dalphinet, A., 2021. Directional and frequency spread of surface ocean waves from swim measurements. Journal of Geophysical Research: Oceans 126, e2021JC017220.

Lee, C., Jung, J.S., Haller, M.C., 2010. Asymmetry in directional spreading function of random waves due to refraction. Journal of waterway, port, coastal, and ocean engineering 136, 1–9.

Lenain, L., Melville, W.K., 2017. Measurements of the directional spectrum across the equilibrium saturation ranges of wind-generated surface waves. Journal of Physical Oceanography 47, 2123–2138.

Longuet-Higgins, M.S., 1963. Observation of the directional spectrum of sea waves using the motions of a floating buoy. Oc. Wave Spectra .

Ludeno, G., Orlandi, A., Lugni, C., Brandini, C., Soldovieri, F., Serafino, F., 2013. X-band marine radar system for high-speed navigation purposes: A test case on a cruise ship. IEEE Geoscience and Remote Sensing Letters 11, 244–248.

Lund, B., Collins, C.O., Graber, H.C., Terrill, E., Herbers, T.H.C., 2014. Marine radar ocean wave retrieval's dependency on range and azimuth. Izv. VUZ. Radiofizika 64, 999–1018.

Lund, B., Collins, C.O., Tamura, H., Graber, H.C., 2016. Multi-directional wave spectra from marine x-band radar. Ocean dynamics 66, 973–988.

Lygre, A., Krogstad, H.E., 1986. Maximum entropy estimation of the directional distribution in ocean wave spectra. Journal of Physical Oceanography 16, 2052–2060.

Mitsuyasu, H., Tasai, F., Suhara, T., Mizuno, S., Ohkusu, M., Honda, T., Rikiishi, K., 1975. Observations of the directional spectrum of ocean wavesusing a cloverleaf buoy. Journal of Physical Oceanography 5, 750 – 760. URL: https://journals.ametsoc.org/view/journals/phoc/5/4/1520-0485_1975_005_0750_ootdso_2_0_co_2.xml, doi:10.1175/1520-0485(1975)005<0750:OOTDSO>2.0.CO;2.

Nieto Borge, J., Guedes Soares, C., 2000. Analysis of directional wave fields using x-band navigation radar. Coastal Engineering 40, 375 – 391. URL: http://www.sciencedirect.com/science/article/pii/S0378383900000193, doi:http://dx.doi.org/10.1016/S0378-3839(00)00019-3.

Nieto-Borge, J., Hessner, K., Jarabo-Amores, P., De La Mata-Moya, D., 2008. Signal-to-noise ratio analysis to estimate ocean wave heights from x-band marine radar image time series. IET Radar, Sonar & Navigation 2, 35–41.

Nieto-Borge, J., Reichert, K., Dittmer, J., 1999. Use of nautical radar as a wave monitoring instrument. Journal of Coastal Engineering 37.

Nieto Borge, J.C., Rodriguez, G.R., Hessner, K., Gonzalez, P.I., 2004. Inversion of marine radar images for surface wave analysis. Journal of Atmospheric and Oceanic Technology 21.

Paláez-Zapata, D., Pakrashi, V., Frédéric, D., 2023. Ocean wave directional spreading from gps-buoy observations off the west coast of ireland: Assessment of a wavelet-based method. Submitted in 2023 .

Plant, W.J., Farquharson, G., 2012. Wave shadowing and modulation of microwave backscatter from the ocean. Journal of Geophysical Research 117, C08010.

Rees, W.G., 2013. Physical Principles of Remote Sensing:. 2 ed., Cambridge University Press, Cambridge. URL: https://www.cambridge.org/core/books/physical-principles-of-remote-sensing/08EBDC7B45B2FC6FCFF1443473C03BAE, doi:10.1017/CBO9780511812903.

Reichert, K., 1994. Analysis of the azimuth dependence of the navigation radar imaging of the sea surface. Diplomarbeit, Fachbereich Geowissenschaften Universitat Hambmg .

Romero, L., Melville, W.K., Kleiss, J.M., 2012. Spectral energy dissipation due to surface wave breaking. Journal of Physical Oceanography 42, 1421–1444.

Seemann, J., Ziemer, F., Senet, M.C., 1997. A method for computing calibrated ocean wave spectra from measurements with a nautical x-band radar, in: IEEE Oceans, pp. 1148–1154.

Senet, M.C., Seemann, J., Ziemer, F., 2001. The near-surface current velocity determined from image sequences of the sea surface. IEEE Transactions on Geoscience and Remote Sensing 39, 492–505.

Støle-Hentschel, S., Borge, J.C.N., Trulsen, K., 2021. The deconvolution as a method to deal with gaps in ocean wave measurements. Ocean Engineering 219, 108373.

Støle-Hentschel, S., Seemann, J., Nieto Borge, J.C., Trulsen, K., 2018. Consistency between sea surface reconstructions from nautical x-band radar doppler and amplitude measurements. Journal of Atmospheric and Oceanic Technology 35, 1201–1220.

Wetzel, L., 1986. On microwave scattering by breaking waves. Wave dynamics and radio probing of the ocean surface , 273–284.

Wyatt, L., Green, J., Gurgel, K.W., Borge, J.N., Reichert, K., Hessner, K., Günther, H., Rosenthal, W., Saetra, O., Reistad, M., 2003. Validation and intercomparisons of wave measurements and models during the eurorose experiments. Coastal Engineering 48, 1–28.

Young, I.R., Rosenthal, W., Ziemer, F., 1985. A three-dimensional analysis of marine radar images for the determination of ocean wave directionality and surface currents. JGR 90, 1049–1059. doi:10.1029/JC090iC01p01049.

Ziemer, F., Dittmer, J., 1994. A system to monitor ocean wave fields, in: Proceedings of OCEANS'94, IEEE. pp. II–28.

Ziemer, F., Günther, H., 1994. A system to monitor ocean wave fields, in: 2nd Int. Conf. Air-Sea Interaction Meteorol. Oceanogr. Coastal Zone.